ACS NANO

www.acsnano.org

ARTICLE

Selective NO_x^- Electroreduction to Ammonia on Isolated Ru Sites

Zunjian Ke,[▽] Dong He,[▽] Xingxu Yan, Wenhui Hu, Nicholas Williams, Hongxing Kang, Xiaoqing Pan, Jier Huang, Jing Gu,* and Xiangheng Xiao*

Cite This: *ACS Nano* 2023, 17, 3483−3491

Read Online

ACCESS | Metrics & More | Article Recommendations | Supporting Information

ABSTRACT: **Nitrate and nitrite (NO_x^-) are widespread contaminants in industrial wastewater and groundwater. Sustainable ammonia (NH_3) production via NO_x^- electroreduction provides a prospective alternative to the energy-intensive industrialized Haber−Bosch process. However, selectively regulating the reaction pathway, which involves complicated electron/proton transfer, toward NH_3 generation relies on the robust catalyst. A specific consideration in designing selective NO_x^--to-NH_3 catalysts should meet the criteria to suppress competing hydrogen evolution and avoid the presence of neighboring active sites that are in favor of adverse N−N coupling. Nevertheless, efforts in this regard are still inadequate. Herein, we demonstrate that isolated ruthenium sites can selectively reduce NO_x^- into NH_3, with maximal Faradaic efficiencies of 97.8% (NO_2^- reduction) and 72.8% (NO_3^- reduction) at −0.6 and −0.4 V, respectively. Density functional theory calculations simulated the reaction mechanisms and identified the *NO → *NOH as the potential rate-limiting step for NO_x^--to-NH_3 conversion on single-atom Ru sites.**

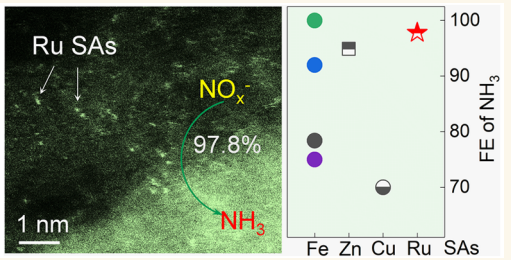

KEYWORDS: *Ammonia electrosynthesis, Nitrate and nitrite, Single-atom Ru sites, Selectivity, Nitrogen cycle*

INTRODUCTION

Ammonia (NH_3), as a fertilizer and basic chemical feedstock, is one of the most valuable and versatile compounds. Also, it has been regarded as a promising energy storage molecule due to its high energy density and carbon-neutrality.[1,2] Nowadays, industrial NH_3 production mainly depends on the conventional Haber−Bosch process. Unfortunately, this process demands large fossil fuel input and high operational costs in order to maintain the high pressure and temperature conditions (Figure 1).[3] The NH_3 manufacturing industry consumes 1−2% of the world's energy supply and accounts for ca. 1% of total global carbon dioxide (CO_2) emissions.[4−6] By contrast, the ambient NH_3 electrosynthesis necessitates only electricity that can be generated from renewable sources, such as solar or wind, providing a sustainable alternative route for the Haber−Bosch approach (Figure 1).[7−11] Currently, for NH_3 electrosynthesis, dinitrogen (N_2) is the main feedstock; however, the reduction of N_2 to NH_3 suffers from extremely low Faradaic efficiencies (FEs) and yields due to the stable and nonpolar nature of the N≡N bond. Fortunately, NH_3 can be produced not only by fixing N_2 but also by converting nitrogenous contaminants.[12,13]

Nitrate and nitrite (NO_x^-), as harmful and toxic contaminants, are extensively found in industrial wastewater and groundwater, due to anthropogenic chemical production and crop fertilization (Figure 1).[14−18] The degradation of NO_x^- from wastewater is an urgent task to restore the globally perturbed nitrogen cycle, while the conventional removal of NO_x^-, known as "denitrification", aims at the reduction of NO_x^- to N_2.[19] The electrochemical conversion from NO_x^- to NH_3 can not only clean wastewater but also generate indispensable NH_3, eliminating drawbacks of the energy-intensive Haber−Bosch method. However, the electroreduction of NO_x^- to NH_3 commonly involves complicated electron and proton transfer,[20−22] arousing a major challenge for improving NH_3 selectivity.[23] Therefore, it is imperative to identify NO_x^- reduction catalysts that are efficient while capable of avoiding the competitive adverse reactions.

Single-atom catalysts (SACs), due to their maximum atom utilization efficiency, distinct activity, and superior selectivity,[24] have emerged as important catalysts for the CO_2 reduction reaction,[25] oxygen reduction reaction,[26] and nitrogen reduction reaction.[27] The rapid development of SACs in these fields suggests that the SACs with superior performance toward

Received: September 28, 2022
Accepted: February 2, 2023
Published: February 6, 2023

https://doi.org/10.1021/acsnano.2c09691
ACS Nano 2023, 17, 3483−3491

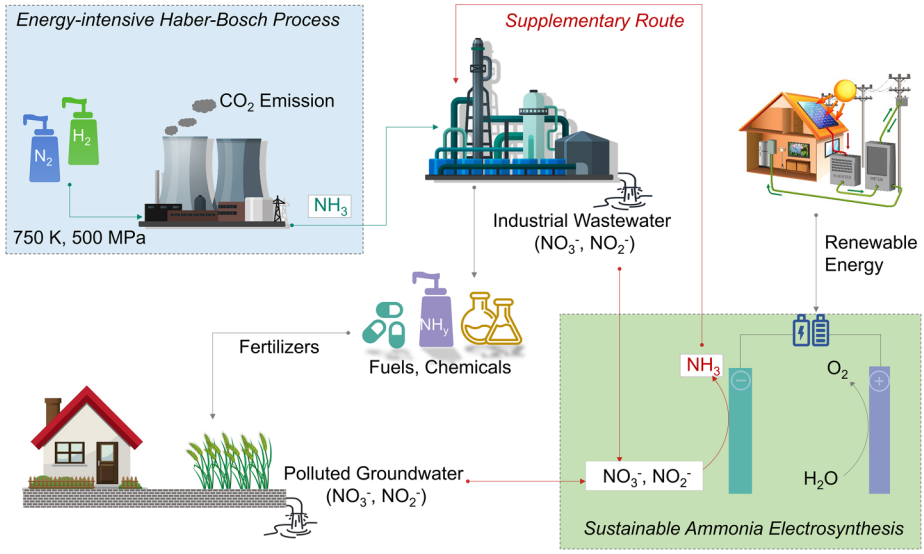

Figure 1. An illustration on proposed nitrogen cycles involving industrial and electrochemical NH_3 synthesis.

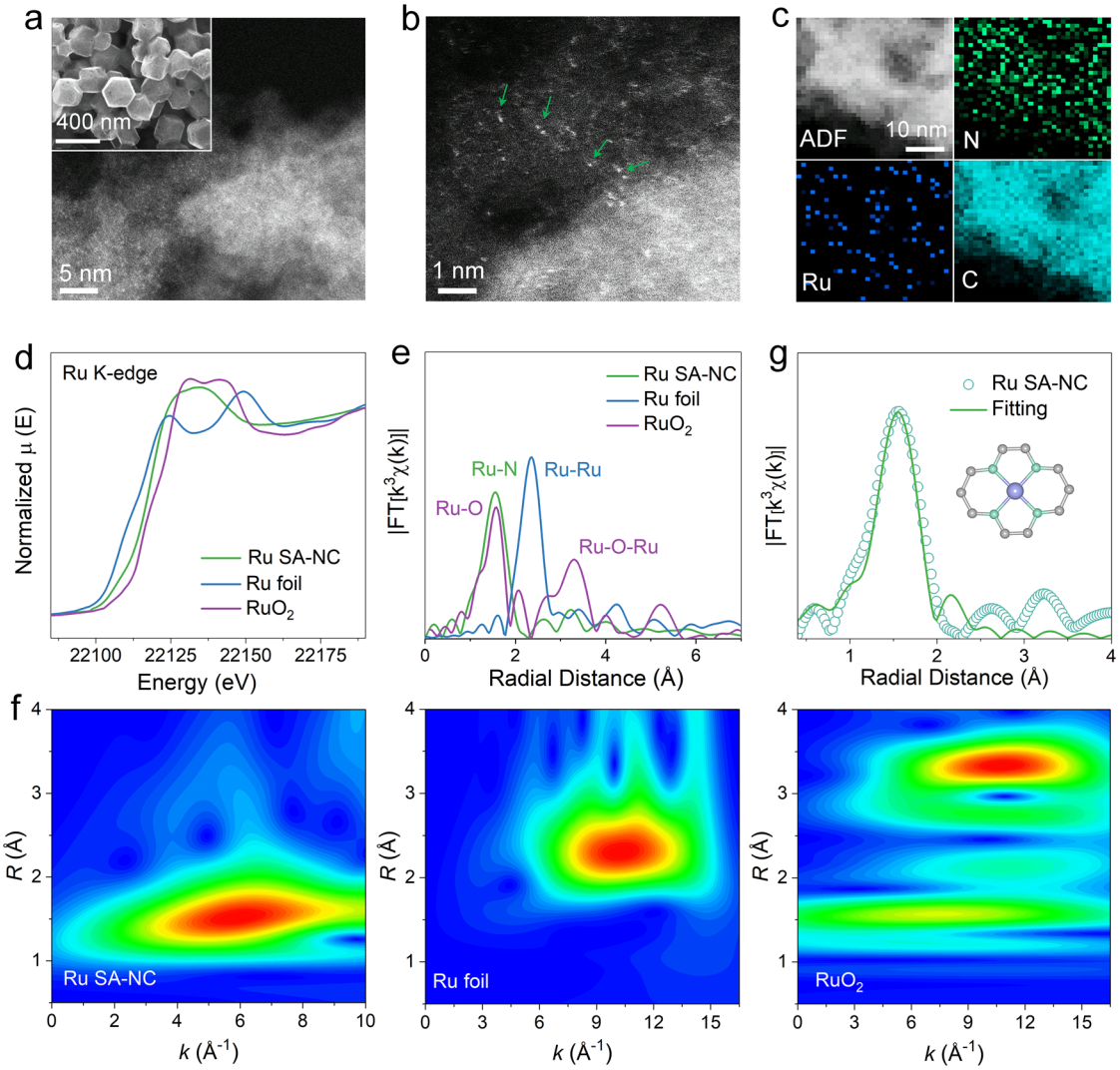

Figure 2. Electron microscopy and X-ray absorption spectroscopy characterizations. (a) HAADF-STEM and SEM (inset) image, (b) atomic resolution HAADF-STEM image, and (c) HAADF image with corresponding EDS elemental mapping for Ru SA-NC. (d) Ru K-edge XANES, (e) Fourier transforms of k^3-weighted Ru K-edge EXAFS, and (f) wavelet transforms of Ru K-edge EXAFS for Ru SA-NC, Ru foil, and RuO_2. (g) EXAFS fitting for the Ru SA-NC.

https://doi.org/10.1021/acsnano.2c09691
ACS Nano 2023, 17, 3483−3491

NO_x^- electroreduction to NH_3 could be designed. More importantly, compared to bulk catalysts with plenty of neighboring active sites, uniformly isolated sites in SACs can generally suppress hydrogen adsorption[28] while preventing the N−N coupling step toward N_2 generation,[29] exhibiting huge potentials for selective NO_x^- electroreduction to NH_3. Up to now, only Fe, Cu, and Zn SACs were reported for NO_3^- reduction to NH_3.[23,29−33] For instance, to mimic the roles of Fe sites in Haber−Bosch catalysts and nitrogenase enzymes, some groups designed Fe SACs which demonstrated excellent performance.[23,29,32] Nevertheless, some of the Fe SACs exhibited sluggish electrocatalytic activity[32] and lower Faradaic efficiencies of NH_3.[29] Wu et al. fabricated Zn SACs for NO_3^- reduction and verified the high NH_3 selectivity (94.8%). However, Zn SACs required a high bias of −0.9 V in order to achieve the good selectivity.[30] Similarly, Cu SACs delivered impressive performance for NO_3^- reduction.[33] Unfortunately, the identification of true active sites raised additional concerns, since metallic Cu nanoparticles were identified during NO_3^- conversion.[34] Hence, further endeavors in exploiting robust and selective single-atom alternatives for NO_x^--to-NH_3 conversion are still highly desired.

Inspired by the Sabatier principle, where Ru locates at the top of the volcano plot for the Haber−Bosch NH_3 synthesis volcano,[35] we demonstrate that atomically dispersed Ru sites loaded on nitrogenated carbon (Ru SA-NC) exhibited impressive activity and NH_3 selectivity for both nitrate and nitrite reduction in basic conditions. The Ru SA-NC catalyst delivered maximal Faradaic efficiencies of 97.8% (NO_2^- reduction) and 72.8% (NO_3^- reduction) toward NH_3 at −0.6 and −0.4 V vs RHE, respectively, which were significantly higher than that of Ru nanoparticles. Density functional theory (DFT) calculations revealed that the *NO → *NOH process, which was identified as a potential rate-limiting step, more favorably occurred on isolated Ru sites.

RESULTS AND DISCUSSION

Synthesis and Characterizations of Ru SA-NC. The Ru SA-NC was synthesized by a metal organic framework assisted self-assembly process in Figure S1. The zeolite imidazolate framework (ZIF-8) was employed as a support to trap $Ru(acac)_3$ precursors to form a Ru-ZIF-8 composite, which was further converted to Ru SA-NC via a high-temperature pyrolysis (see the Methods section). The Ru mass loading in the final Ru SA-NC was determined to be 0.322% by the inductively coupled plasma optical emission spectroscopy (ICP-OES). X-ray diffraction (XRD) of ZIF-8 and Ru-ZIF-8 in Figure S2a showed similar patterns with characteristic peaks consistent with previous works,[36,37] indicating the ZIF-8 was well fabricated and Ru sources were uniformly incorporated into the ZIF-8 host. After the pyrolysis, both NC and Ru SA-NC exhibited amorphous features (Figure S2b) with no characteristic crystalline Ru peaks (Figure S2c), suggesting possible formations of isolated Ru sites in Ru SA-NC. Additionally, the defect states caused by the evaporation of the Zn center in ZIF-8 were verified by Raman spectra and X-ray photoelectron spectroscopy (XPS) in Figures S3 and S4, where the peaks at 398.5, 400.0, 401.1, and 402.8 eV in N 1s of Ru SA-NC were indexed to pyridinic, pyrrolic, graphitic, and oxidized N, respectively, indicating the organic linkers of ZIF-8 were converted to nitrogen-doped carbon.[37,38] In order to further confirm the successful preparation of the catalysts, the morphological and structural properties of Ru SA-NC were investigated via electronic microscopic methods. Scanning electron microscopy (SEM) and transmission electron microscopy (TEM) images revealed that both Ru-ZIF-8 and Ru SA-NC exhibited homogeneous rhomb dodecahedral morphologies, and the rhomb-dodecahedrons for Ru SA-NC exhibited smaller sizes and a more porous surface than those of Ru-ZIF-8 due to the pyrolysis (Figures S5 and S6). Scanning transmission electron microscopy (STEM) was performed to identify the presence and distribution of Ru single atoms. The STEM images in Figure S7a,b revealed typical amorphous and porous morphologies of Ru SA-NC, and the high-angle annular dark field (HAADF) STEM images uncovered that there were no obvious Ru nanoparticles in the sample (Figure 2a, Figure S7c). Atomically dispersed Ru species were further identified by sub-angstrom HAADF images in Figure 2b and Figure S8, where plenty of isolated bright spots (green arrows) were distributed throughout the sample, confirming the presence of Ru single atoms. Energy-dispersive X-ray spectroscopy (EDS) with corresponding elemental mapping further verified the presence of Ru, N, and C (Figure 2c, Figure S9). Additionally, STEM and EDS results in Figures S10 and S11 showed that the Ru NPs, used for comparison with Ru SA-NC, were well synthesized, and the crystalline nature of Ru NPs was uncovered by HAADF-STEM images in Figure S12.

The electronic and coordination structures of Ru single atoms were further investigated by X-ray absorption spectroscopy (XAS). Ru K-edge X-ray absorption near edge spectroscopy (XANES) of Ru SA-NC in Figure 2d exhibited higher absorption energy and stronger white-line intensity than that of Ru foil, suggesting that Ru in Ru SA-NC was positively charged.[37] Here, Ru SA-NC exhibited a similar energy absorption edge profile with that of the $Ru(acac)_3$ reference from 22100 to 22120 eV (Figure S13a); together, the derivative profile of XANES for Ru SA-NC also showed a similar pre-edge structure with that of $Ru(acac)_3$ from 22103 to 22108 eV (Figure S13b), suggesting the valence state of single-atom Ru was ∼ +3. Further, Ru K-edge X-ray absorption fine structure spectroscopy (EXAFS) for Ru SA-NC in Figure 2e presented a predominant peak around 1.5 Å, which was attributed to the existence of Ru−N bonds. There were no obvious peaks from metallic Ru (∼2.4 Å for Ru−Ru scattering in Ru foil) and oxidized Ru species (∼1.55 Å for Ru−O and ∼3.3 Å for Ru−O−Ru bonds in RuO_2),[36,37] indicating the presence of isolated Ru sites with Ru−N coordination. Furthermore, the wavelet analysis of the EXAFS in Figure 2f showed that Ru foil exhibited a maximal intensity at 10 $Å^{-1}$, which was assigned to the metallic Ru−Ru scattering. The RuO_2 had an intensity maximum at 10.5 $Å^{-1}$ derived from Ru−O−Ru contributions, whereas the Ru-SA-NC showed only one intensity maximum at a much lower *k*-space of 5.5 $Å^{-1}$ due to the Ru−N contribution.[34] These results indicated that the Ru in Ru SA-NC was presented as a mononuclear Ru center. We further conducted EXAFS fitting analysis (Figure 2g, Figure S14, Table S1) and revealed the presence of the Ru−N scattering path with a coordination number of 4.0 and a Ru−N bond length of 2.11 Å, indicating the Ru−N_4 configuration of isolated Ru sites in Ru SA-NC (Figure 2g).

Electrocatalytic NO_x^- Reduction Performance. Electrocatalytic NO_x^- reduction performance of Ru SA-NC was investigated in an H-cell with a typical three-electrode configuration (see the Methods section). As shown in Figure S15, the linear sweep voltammetry (LSV) tests in pure 1.0 KOH solution revealed the sluggish HER activity of Ru SA-

https://doi.org/10.1021/acsnano.2c09691
ACS Nano 2023, 17, 3483−3491

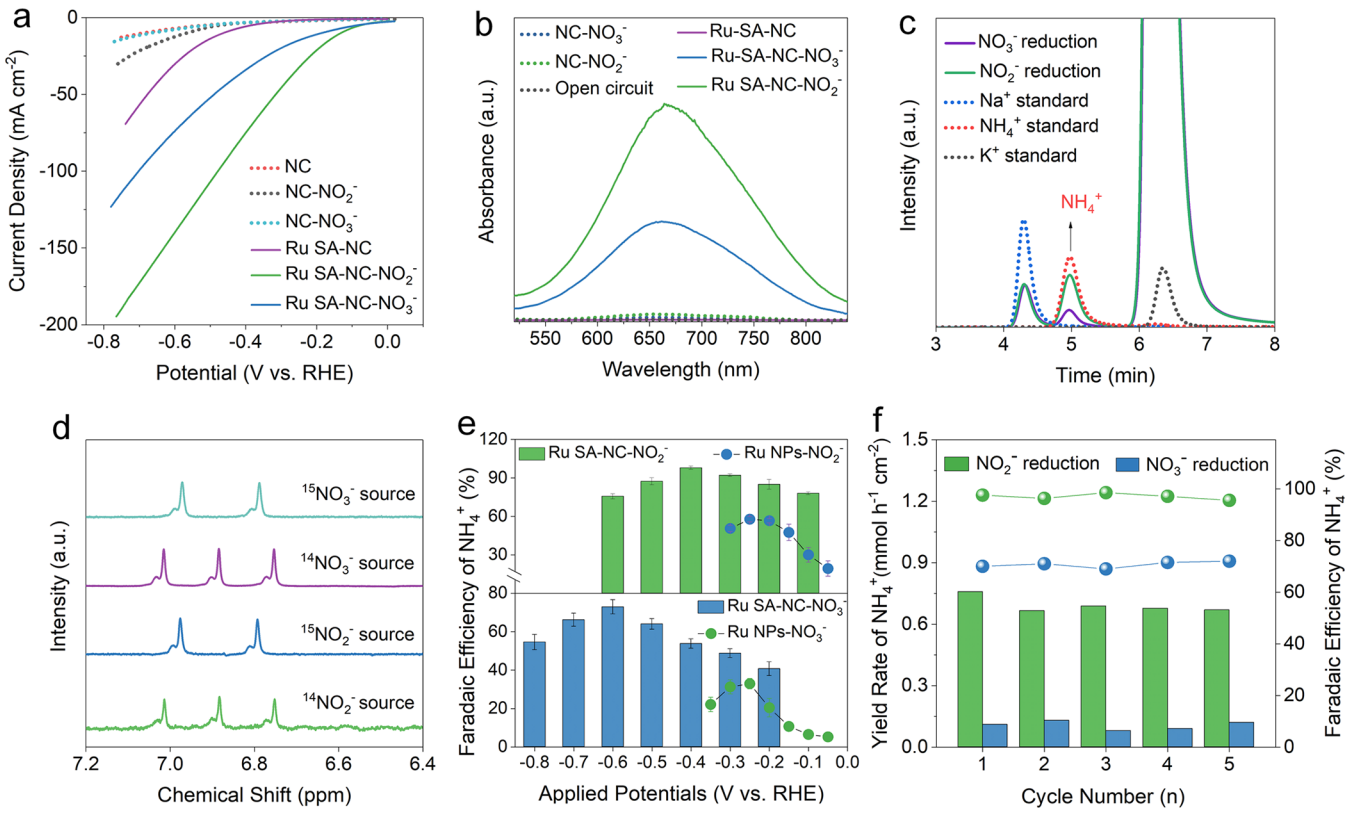

Figure 3. Electrocatalytic NO_x^- reduction performance. (a) LSV plots of NC and Ru SA-NC in 1.0 M KOH electrolytes with and without 0.5 M NO_3^- or NO_2^-. (b) UV−visible absorption spectra of the electrolytes under various operational conditions. (c) Ion chromatography (IC) verification of ammonia produced from NO_3^- and NO_2^- reduction catalyzed by Ru SA-NC. Na^+ was from the impurity in KOH. (d) ^{15}N isotope labeling experiments based on NMR measurements. (e) Faradaic efficiencies of ammonia from NO_3^- and NO_2^- reduction over Ru SA-NC and Ru NPs. (f) Yield rates and Faradaic efficiencies of ammonia during 5 successive electrolysis cycles.

NC. The high overpotential of ∼0.5 V indicated that the adverse HER was not favorable on Ru SA-NC. After adding various concentrations of NO_x^- into the electrolytes, the current densities of Ru SA-NC were significantly enhanced, indicating its excellent activity toward NO_x^- reduction. To confirm that the robust activity was attributed to single-atom Ru sites, we compared the catalytic activities of NC and Ru SA-NC in Figure 3a and Figure S16. NC exhibited negligible activity for both NO_3^- and NO_2^- reduction, while Ru SA-NC presented sharply escalated current densities and decreased onset potentials, suggesting that the presence of isolated Ru sites significantly improved NO_x^- reaction activity. Additionally, the NO_x^- reduction performance of Ru NPs was also investigated for comparison with Ru SA-NC (Figure S17). Although Ru NPs exhibited slightly better activities for both NO_3^- and NO_2^- reduction than those of Ru SA-NC, Ru NPs delivered a significantly higher current density of HER than Ru SA-NC. Considering the competition between HER and NO_x^- reduction, accurate evaluations of NO_x^- reduction performance are dependent upon the quantitation analysis of products. The products of NO_x^- reduction were analyzed by the indophenol blue method in combination with the UV−vis absorption spectroscopy (Figure 3b). The UV−vis spectrum of the electrolyte at open circuit did not show any appearance of ammonia, indicating that there was no ammonia impurity in the initial electrolyte. Similarly, no ammonia was detected after 2 h electrolysis of the electrolyte without NO_x^-. This result confirmed that the ammonia, produced from the possible nitrogen-containing species in the Ru SA-NC, was negligible. After adding 0.5 M NO_3^- or NO_2^-, the UV−vis spectra of the electrolytes after 2 h electrolysis by Ru SA-NC exhibited strong ammonia absorptions at ∼663 nm, whereas the ammonia absorptions were pretty weak after the electrolysis by NC. This result suggested that single-atom Ru sites are capable of effectively reducing NO_x^- to ammonia, corresponding well with LSV results in Figure 3a. The produced ammonia was further confirmed by ion chromatography (IC) and ^1H nuclear magnetic resonance (NMR) (Figure 3c,d, Figure S18). The peak that presented around 5 min in IC was assigned to NH_4^+. The ^1H NMR spectra (pink and green) exhibited a typical three-peak pattern,[12,28,29,36,37,39,40] suggesting the generation of ammonia. Subsequently, nitrogen isotope labeling (^{15}N) experiments were conducted to track the nitrogen source. The NMR spectra in Figure 3d (blue and light green) exhibited only two peaks, validating that the ammonia originated from NO_x^- instead of other nitrogen-containing species.[12,39,40] To further investigate the selectivity of the catalysts, Faradaic efficiencies (FEs) were quantified based on a calibrated ammonia concentration curve (Figure S19). As presented in Figure 3e, at lower potentials, Ru SA-NC delivered gradually increased ammonia FEs for both NO_3^- and NO_2^- reduction. The maximal FEs for NO_3^- and NO_2^- reduction were 72.8% at −0.6 V and 97.8% at −0.4 V, respectively. Beyond those potentials, the FEs decreased, which was ascribed to the acceleration of the competing HER. Compared with Ru SA-NC, NC exhibited negligible ammonia selectivity (Figure S20), indicating that the role of possible Zn residue after the pyrolysis was insignificant. Moreover, Ru NPs

https://doi.org/10.1021/acsnano.2c09691
ACS Nano 2023, 17, 3483−3491

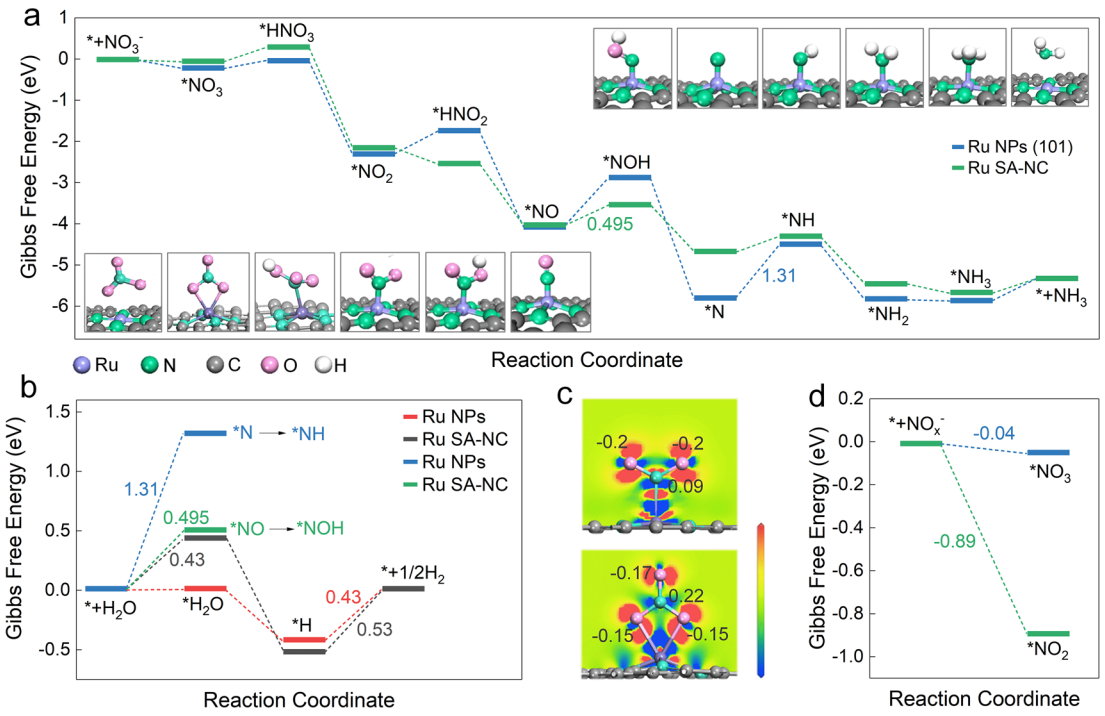

Figure 4. DFT calculations. (a) Gibbs free energy diagrams of NO_x^- reduction to ammonia on Ru SA-NC and Ru NPs. The inset was the optimized intermediate adsorption configurations. (b) The Gibbs free energy comparison for key steps of NO_x^- reduction and HER on Ru SA-NC and Ru NPs. (c) The optimized charge density difference of Ru SA-NC after NO_3^- and NO_2^- adsorptions. All values represent the Hirshfeld charge. The scale from red to blue was 0.05 to −0.05 e^{-1}. (d) Gibbs free energy diagrams of NO_x^- adsorptions on Ru SA-NC.

delivered significantly lower FEs for both NO_3^- (32.9% maximal at −0.25 V) and NO_2^- (57.8% maximal at −0.25 V), which was as expected, since Ru NP was a superior HER catalyst (Figure 3e).[37] In addition, we calculated the partial current densities of ammonia produced on Ru SA-NC and Ru NPs (Figure S21). Although Ru NPs exhibited higher total current densities, their partial densities for ammonia were lower than that of Ru SA-NC, further revealing the superior ammonia selectivity of the Ru SA-NC. The durability of the Ru SA-NC was evaluated through successive electrolysis. After five successive cycles, the FE of Ru SA-NC remained nearly unchanged, indicating its superior stability. The average ammonia FEs for NO_3^- and NO_2^- reduction were 70.7 and 97.0%, respectively, and the corresponding average ammonia yield rates were 0.69 and 0.11 mmol h^{-1} cm^{-2} (Figure 3f). These properties were superior to most of the NO_x^- reduction and N_2 fixation catalysts (Table S2, Table S3).[40−47]

DFT Investigations. DFT simulations were performed to unravel the NO_x^- reduction reaction mechanism and the origin of Ru SA-NC's superior performance (see the Methods section). According to our experimental results (Figure 2, Figure S2), the Ru−N_4 site was used as the computational model, and the Ru NPs (101) as Ru^0 sites were also modulated for comparison. We first calculated the Gibbs free energy of the intermediates during NO_x^- reduction on Ru−N_4 and Ru^0 sites in Figure 4a. The reaction pathway for the calculations was based on the optimized reaction routes in the literature where NO_x^- was reduced to ammonia through deoxygenation and protonation processes.[23,39] As displayed in Figure 4a, the NO_3^- was first adsorbed on the surface to form $*NO_3$, which was then converted to $*HNO_3$ through a solution-mediated protonation step. The $*HNO_3$ was then reduced to $*NO_2$ and transformed into $*HNO_2$ via a hydrogenation process. Subsequently, $*HNO_2$ dissociated to *NO, which was the key intermediate for NO_x^- reduction on Ru−N_4 sites. The further reduction of *NO to *NOH on Ru−N_4 was significantly uphill (0.495 eV) in free energy, which was identified as the rate-limiting step. However, the *NO → *NOH step on Ru^0 sites exhibited a higher barrier (1.20 eV) than that of the Ru−N_4 sites, indicating the formation of the *NOH intermediate was more favorable on Ru SA-NC. Compared with Ru SA-NC, the rate-limiting step of NO_x^- reduction on Ru NPs was determined to be the *N → *NH process with an increased free energy of 1.31 eV, which was sharply higher than that of the Ru SA-NC. These findings uncovered the origin of the superior performance of Ru SA-NC in comparison with Ru NPs. Furthermore, considering the effect of the electrode potential on the protonation steps, we provided potential-calibrated DFT calculation results in Figure S22. When the electrode potential was set to −0.495 V vs NHE, the ΔG of all electrochemical steps for NO_x^- reduction on Ru SA-NC was ≤0 eV, whereas the ΔG of the *N → *NH step for NO_x^- reduction on Ru NPs was still up to 1.11 eV. Again, the potential-calibrated DFT results together with our previous results all demonstrated the beneficial energetics of Ru SA-NC for NO_x^- reduction. To further elaborate on this point, we compared the free energy diagram for key steps of NO_x^- reduction and water dissociation on Ru SA-NC and Ru NPs. As shown in Figure 4b, for Ru SA-NC, the free energy change (ΔG) for the *H desorption was 0.53 eV, higher than ΔG of *NO → *NOH, suggesting that the NO_x^- reduction was more energetically favorable than HER. Nevertheless, the ΔG of the *N → *NH step for Ru NPs was 1.31 eV, significantly higher than that of *H desorption (0.43 eV). These results demonstrated that the HER was more preferred than NO_x^- reduction on the Ru^0 sites. Thus, Ru NPs exhibited

https://doi.org/10.1021/acsnano.2c09691
ACS Nano 2023, 17, 3483−3491

a higher HER activity and a lower NH_3 selectivity. In conclusion, these DFT results provided sufficient evidence for understanding the superior selectivity of Ru SA-NC for NO_x^- reduction. Additionally, we have further compared the NO_3^- and NO_2^- adsorption properties on Ru SA-NC in Figure 4c,d. The charge density differences on the Ru−N_4 sites after NO_3^- and NO_2^- adsorption (Figure 4c) indicated that the Ru−N_4 sites would exhibit higher NO_2^- reduction activity than NO_3^- reduction, corresponding well with the experimental results in Figure 3. Further, this result was verified by the Gibbs free energy change for NO_x^- adsorption in Figure 4d.

CONCLUSIONS

In summary, we have demonstrated Ru single atoms as an active and selective electrocatalyst to reduce nitrate and nitrite to valuable ammonia. In comparison to Ru NPs, atomically dispersed Ru sites, with unique coordination environments and electronic structures, delivered much higher catalytic activities and selectivity for NO_x^- reduction. DFT calculations revealed the possible rate-determining steps in NO_x^- reduction and elucidated why the isolated Ru sites exhibited superior performance in thermodynamics. The nitrogen cycle is one of the most important biogeochemical cycles that balance the nitrogen species on the earth. The ability to convert NO_x^- back into ammonia will facilitate closing the nitrogen cycle for green wastewater purification and sustainable ammonia production.

METHODS

Chemicals. Zinc nitrate hexahydrate (Zn $(NO_3)_2{\cdot}6H_2O$), 2-methyl imidazole (2-MeIM), ruthenium(III) acetylacetonate (Ru-$(acac)_3$), ammonium chloride (NH_4Cl), ammonium-^{15}N chloride ($^{15}NH_4Cl$), potassium hydroxide (KOH), sodium hypochlorite solution (NaClO, available chlorine 4−4.99%), sodium nitrite-^{15}N ($Na^{15}NO_2$), and sodium nitrate-^{15}N ($Na^{15}NO_3$) were purchased from Sigma-Aldrich. Methanol, sulfuric acid (H_2SO_4, 96−98%), sodium hydroxide (NaOH), deuterium oxide (D_2O), and Nafion D-520 dispersion were from Fisher Chemical. Potassium sodium tartrate tetrahydrate ($KNaC_4H_{12}O_{10}{\cdot}4H_2O$) and sodium nitroferricyanide dihydrate ($C_5FeN_6Na_2O{\cdot}2H_2O$) were from Acros Organics. Salicylic acid ($C_7H_6O_3$) and sodium nitrate ($NaNO_3$) were from Alfa Aesar. Sodium nitrite ($NaNO_2$) was from Merck KGaA. All chemicals were directly used without further purifications.

Synthesis of Ru-ZIF-8, Ru SA-NC, Ru NPs, ZIF-8, and NC. In a typical synthesis,[37] 2.976 g Zn $(NO_3)_2{\cdot}6H_2O$ and 0.1 g Ru$(acac)_3$ were dissolved in 80 mL methanol, which was subsequently added into 80 mL methanol containing 3.29 g 2-methyimidazole. After sonicating for 15 min, the mixture was under static at room temperature for 24 h. The as-obtained precipitate was centrifuged and washed with methanol three times and then dried in a vacuum at 65 °C overnight. The obtained pink powder was denoted as Ru-ZIF-8. To prepare Ru SA-NC, the Ru-ZIF-8 was annealed at 1000 °C for 2 h with a ramping rate of 5 °C min^{-1} in a nitrogen flow. Then, the as-obtained black powder was soaked in 1.0 M H_2SO_4 solution for 5 h to remove the unstable oxidative species. The precipitate was washed with deionized water several times and dried in a vacuum at 65 °C overnight. The obtained sample was denoted as Ru SA-NC and directly used for the catalytic tests without further treatment. The synthetic procedures of ZIF-8 and NC were similar to those of Ru-ZIF-8 and Ru SA-NC except for removing the Ru source. Ru NPs were synthesized according to similar procedures except for adding 0.3 g Ru$(acac)_3$.

Material Characterizations. The crystal structures of the samples were characterized by X-ray diffraction technology (XRD) with PANalytical X'Pert using Cu Ka radiation (λ = 1.5418 Å). The morphologies of samples were visualized by scanning electron microscopy (SEM) using a FEI Quanta 450 SEM operated at 25 kV. Scanning transmission electron microscopy (STEM, JEOL Grand) was performed to observe the morphologies of samples and distribution of single atoms, and the high-angle angular dark-filled (HAADF)-STEM images were acquired by a convergence semiangle of 22 mrad and inner and outer collection angles of 83 and 165 mrad, respectively. Energy dispersive X-ray spectroscopy (EDS) was conducted to analyze the element distribution using JEOL dual EDS detectors and a specific high count analytical TEM holder. ICP-OES was conducted on an Agilent 5110.

XAS Measurements. The X-ray absorption structure (XAS) spectra at the Ru K-edge were performed at beamline 12-BM at the Advanced Photon Source, Argonne National Laboratory. The XAS data were recorded under fluorescence mode using a 13-element germanium solid state detector (Canberra). The absorption spectrum of reference Ru foil was collected in the transmission mode with ion chambers for energy calibration. The raw XAS data were averaged, calibrated according to the Ru foil reference, and normalized in Athena. The Fourier-transformed profile of the first shell was fitted using Artemis.

Electrochemical Measurements of Nitrite and Nitrate Reduction. All electrochemical tests were carried out on an electrochemical workstation (CHI 660, Chenhua) with a typical three-electrode configuration where Ag/AgCl, Pt foil, and the catalyst were used as the reference, counter, and working electrode, respectively. For working electrode fabrication, typically, 5 mg samples were dispersed in 1 mL ethanol with 50 μL Nafion D-520 dispersion by sonicating for 1 h. The working electrodes were fabricated via drop-casting 50 μL of the well-dispersed catalyst ink on the carbon paper support (1 × 2 cm^2). After drying naturally in the air, the working electrodes were directly used for electrochemical measurements. 1.0 M KOH aqueous solution with 0.5 M sodium nitrite and sodium nitrate were used as electrolytes for all electrochemical NO_x^- reduction tests. All electrolyte solutions were purged with pure argon flow (50 s.c.c.m.) for 1 h to remove the possibly dissolved CO_2, N_2, and O_2 before electrochemical measurements. All potentials versus Ag/AgCl were calibrated to the reversible hydrogen electrode (RHE) according to the equation

$$E_{RHE} = E_{Ag/AgCl} + 0.059pH + 0.197$$

Ammonia Detection and Faradaic Efficiency Calculation. The produced ammonia was detected by the indophenol blue method and ion chromatography (IC). In a typical indophenol blue method,[12] the coloring agent contained 0.36 M NaOH, 0.36 M salicylic acid, and 0.18 M $KNaC_4H_{12}O_{10}{\cdot}4H_2O$. To prepare the agent to be detected, 4 mL diluted electrolytes was mixed with 500 μL coloring agent, 50 μL 0.034 M $C_5FeN_6Na_2O{\cdot}2H_2O$ solution, and 50 μL NaClO solution containing 0.75 M NaOH. After a complete coloring reaction, the mixture was collected to a cuvette for ultraviolet−visible (UV−vis) spectrophotometry measurements. The measured absorbance was used to calculate the concentration of ammonia according to the standard concentration curve. The standard concentration curve was acquired via similar procedures. The NH_4Cl solutions with various concentrations (0.01, 0.02, 0.05, 0.10, and 0.20 mM) were prepared for UV−vis tests according to the above steps. The standard concentration curve was obtained via a linear fitting of various concentrations and corresponding absorbances. The ammonia concentrations obtained from the above standard curve concentrations were used to calculate the Faradaic efficiencies (FEs) of the ammonia produced from NO_x^- reduction. In addition, the presence of ammonia was further verified by IC (Wayeal, IC 6100). The total reactions of nitrite and nitrate reductions were shown in the following:

$$NO_2^- + 6e^- + 6H_2O = NH_4^+ + 8OH^-$$

$$NO_3^- + 8e^- + 7H_2O = NH_4^+ + 10OH^-$$

https://doi.org/10.1021/acsnano.2c09691
ACS Nano 2023, 17, 3483−3491

Therefore, the FEs of ammonia produced from nitrite and nitrate were calculated according to the equations, respectively,

$$FE_1 = (6C_1 \cdot V \cdot e \cdot N_A)/Q_1$$

$$FE_2 = (8C_2 \cdot V \cdot e \cdot N_A)/Q_2$$

where FE_1 and FE_2 and C_1 and C_2 are the Faradaic efficiencies (%) and molar concentrations ($mol \cdot L^{-1}$) of ammonia produced from NO_2^- and NO_3^-, respectively. Q_1 and Q_2 are the charges (C) transferred during NO_2^- and NO_3^- electrolysis, respectively. e is the elementary charge (1.6×10^{-19} C), N_A is the Avogadro constant (6.022×10^{23}), and V is the volume (L) of the electrolytes.

^{15}N Isotope Labeling Experiments. The ^{15}N isotope labeling experiment was carried out to track the path of N in produced ammonia. To demonstrate that the nitrogen atoms in the produced ammonia were derived from NO_x^- reduction, the 1.0 M aqueous KOH with 0.5 M $Na^{15}NO_2$ or $Na^{15}NO_3$ was used as the electrolyte for electrolysis, respectively. The electrolytes after 2 h electrolysis were collected for ^{1}H nuclear magnetic resonance (NMR) measurements. The NMR samples contain 500 μL electrolytes, 60 μL D_2O (lock-field agent), and 40 μL 10 mM maleic acid (internal standard). For comparison, the NMR data for electrolytes using $Na^{14}NO_2$ and $Na^{14}NO_3$ as nitrogen sources were also collected. All ^{1}H NMR spectra were recorded on Varian spectrometers at 400 MHz.

Density Function Theory (DFT) Calculations. All DFT simulations in this work were conducted using CASTEP code implemented in the Materials Studios package of Accelrys Inc. The electron exchange-correlation potential was conducted by the Perdew–Burke–Ernzerhof (PBE) functional of the generalized gradient approximation (GGA). The ultrasoft pseudopotentials were employed, and the core electrons of atoms were treated using the effective core potential (ECP). For Ru SA-NC, the kinetic energy cutoff was set to 500 eV for the plane-wave basis set. The Brillouin zone integration was sampled with a $4 \times 4 \times 1$ Monkhorst–Pack mesh k-point. The energetic and force tolerances were set to 1×10^{-5} eV/atom and 0.005 eV/Å. Considering the larger lattice vector of Ru NPs, the k-point and plane-wave cutoff were set to $3 \times 2 \times 1$ and 500 eV, respectively. The free energy (ΔG) calculations of each elementary step were based on the standard hydrogen electrode model, which can be determined as

$$\Delta G = \Delta E + \Delta E_{ZPE} - T \cdot \Delta S$$

where ΔE and ΔS are the reaction energy and entropy change and ΔE_{ZPE} is the difference in zero-point energy between the adsorbed and gas phase molecules.

ASSOCIATED CONTENT

Supporting Information

The Supporting Information is available free of charge at https://pubs.acs.org/doi/10.1021/acsnano.2c09691.

Schematic diagram of the material synthesis, XRD, Raman spectroscopy, XPS, SEM, TEM, HAADF-STEM, STEM-EDS, XAS fitting parameters, electrocatalytic performance, and DFT details (PDF)

AUTHOR INFORMATION

Corresponding Authors

Jing Gu − *Department of Chemistry and Biochemistry, San Diego State University, San Diego, California 92182-1030, United States;* orcid.org/0000-0002-5506-0049; Email: jgu@sdsu.edu

Xiangheng Xiao − *Department of Physics, Zhongnan Hospital of Wuhan University, Wuhan University, Wuhan, Hubei 430072, China;* orcid.org/0000-0001-9111-1619; Email: xxh@whu.edu.cn

Authors

Zunjian Ke − *Department of Physics, Zhongnan Hospital of Wuhan University, Wuhan University, Wuhan, Hubei 430072, China*

Dong He − *Department of Physics, Zhongnan Hospital of Wuhan University, Wuhan University, Wuhan, Hubei 430072, China*

Xingxu Yan − *Department of Materials Science and Engineering, University of California, Irvine, Irvine, California 92697, United States;* orcid.org/0000-0001-7991-4849

Wenhui Hu − *Department of Chemistry, Marquette University, Milwaukee, Wisconsin 53201, United States*

Nicholas Williams − *Department of Chemistry and Biochemistry, San Diego State University, San Diego, California 92182-1030, United States*

Hongxing Kang − *Department of Chemistry and Biochemistry, San Diego State University, San Diego, California 92182-1030, United States*

Xiaoqing Pan − *Department of Materials Science and Engineering, University of California, Irvine, Irvine, California 92697, United States; Department of Physics and Astronomy and Irvine Materials Research Institute, University of California, Irvine, Irvine, California 92697, United States;* orcid.org/0000-0002-0965-8568

Jier Huang − *Department of Chemistry, Marquette University, Milwaukee, Wisconsin 53201, United States;* orcid.org/0000-0002-2885-5786

Complete contact information is available at: https://pubs.acs.org/10.1021/acsnano.2c09691

Author Contributions

$^{\nabla}$Z.K. and D.H. contributed equally.

Notes

The authors declare no competing financial interest.

ACKNOWLEDGMENTS

This work was supported by the National Natural Science Foundation of China (12025503, U1932134, U1867215, 12105208), the Fundamental Research Funds for the Central Universities of China (2042021kf0068, 2042022kf1181), and China Postdoctoral Science Foundation (No. 2020M682469). The DFT calculations in this paper were performed on the supercomputing system in the Supercomputing Center of University of Science and Technology of China. J.G. acknowledges the financial support received from National Science Foundation (NSF) award CHE 2154837. The authors acknowledge the use of facilities and instrumentation at the Irvine Materials Research Institute supported in part by NSF through the University of California Irvine Materials Research Science and Engineering Center (DMR-2011967) and the Major Research Instrumentation Program (CHE-1338173). Use of the Advanced Photon Source in Argonne National Laboratory was supported by the U.S. Department of Energy, Office of Science, Office of Basic Energy Sciences, under Award No. DE-AC02-06CH11357.

REFERENCES

(1) Ashida, Y.; Arashiba, K.; Nakajima, K.; Nishibayashi, Y. Molybdenum-catalysed ammonia production with samarium diiodide and alcohols or water. *Nature* **2019**, *568* (7753), 536–540.

(2) Foster, S. L.; Bakovic, S. I. P.; Duda, R. D.; Maheshwari, S.; Milton, R. D.; Minteer, S. D.; Janik, M. J.; Renner, J. N.; Greenlee, L.

F. Catalysts for nitrogen reduction to ammonia. *Nat. Catal.* **2018**, *1* (7), 490−500.
(3) Van Langevelde, P. H.; Katsounaros, I.; Koper, M. T. M. Electrocatalytic nitrate reduction for sustainable ammonia production. *Joule* **2021**, *5* (2), 290−294.
(4) Tang, C.; Qiao, S. Z. How to explore ambient electrocatalytic nitrogen reduction reliably and insightfully. *Chem. Soc. Rev.* **2019**, *48* (12), 3166−3180.
(5) Suryanto, B. H. R.; Du, H.-L.; Wang, D.; Chen, J.; Simonov, A. N.; MacFarlane, D. R. Challenges and prospects in the catalysis of electroreduction of nitrogen to ammonia. *Nat. Catal.* **2019**, *2* (4), 290−296.
(6) Guo, C.; Ran, J.; Vasileff, A.; Qiao, S. Z. Rational design of electrocatalysts and photo(electro)catalysts for nitrogen reduction to ammonia (NH_3) under ambient conditions. *Energy Environ. Sci.* **2018**, *11* (1), 45−56.
(7) Chen, P.; Zhang, N.; Wang, S.; Zhou, T.; Tong, Y.; Ao, C.; Yan, W.; Zhang, L.; Chu, W.; Wu, C.; Xie, Y. Interfacial engineering of cobalt sulfide/graphene hybrids for highly efficient ammonia electrosynthesis. *Proc. Natl. Acad. Sci. U.S.A.* **2019**, *116* (14), 6635−6640.
(8) Wang, J.; Yu, L.; Hu, L.; Chen, G.; Xin, H.; Feng, X. Ambient ammonia synthesis via palladium-catalyzed electrohydrogenation of dinitrogen at low overpotential. *Nat. Commun.* **2018**, *9* (1), 1795.
(9) Song, Y.; Johnson, D.; Peng, R.; Hensley, D. K.; Bonnesen, P. V.; Liang, L.; Huang, J.; Yang, F.; Zhang, F.; Qiao, R. A physical catalyst for the electrolysis of nitrogen to ammonia. *Sci. Adv.* **2018**, *4* (4), No. e1700336.
(10) Cui, X.; Tang, C.; Zhang, Q. A Review of Electrocatalytic Reduction of Dinitrogen to Ammonia under Ambient Conditions. *Adv. Energy Mater.* **2018**, *8* (22), 1800369.
(11) Chen, G. F.; Cao, X.; Wu, S.; Zeng, X.; Ding, L. X.; Zhu, M.; Wang, H. Ammonia Electrosynthesis with High Selectivity under Ambient Conditions via a Li^+ Incorporation Strategy. *J. Am. Chem. Soc.* **2017**, *139* (29), 9771−9774.
(12) Wang, Y.; Xu, A.; Wang, Z.; Huang, L.; Li, J.; Li, F.; Wicks, J.; Luo, M.; Nam, D. H.; Tan, C. S.; Ding, Y.; Wu, J.; Lum, Y.; Dinh, C. T.; Sinton, D.; Zheng, G.; Sargent, E. H. Enhanced nitrate-to-ammonia activity on copper-nickel alloys via tuning of intermediate adsorption. *J. Am. Chem. Soc.* **2020**, *142* (12), 5702−5708.
(13) Li, H.; Yan, C.; Guo, H.; Shin, K.; Humphrey, S. M.; Werth, C. J.; Henkelman, G. Cu_xIr_{1-x} nanoalloy catalysts achieve near 100% selectivity for aqueous nitrite reduction to NH_3. *ACS Catal.* **2020**, *10* (14), 7915−7921.
(14) Kanter, D. R.; Chodos, O.; Nordland, O.; Rutigliano, M.; Winiwarter, W. Gaps and opportunities in nitrogen pollution policies around the world. *Nat. Sustain.* **2020**, *3* (11), 956−963.
(15) Zhu, X.; Zeng, X. C.; Chen, X.; Wu, W.; Wang, Y. Inhibitory effect of nitrate/nitrite on the microbial reductive dissolution of arsenic and iron from soils into pore water. *Ecotoxicology* **2019**, *28* (5), 528−538.
(16) Martínez, J.; Ortiz, A.; Ortiz, I. State-of-the-art and perspectives of the catalytic and electrocatalytic reduction of aqueous nitrates. *Appl. Catal. B: Environ.* **2017**, *207*, 42−59.
(17) Elmi, A. A.; Madramootoo, C.; Egeh, M.; Hamel, C. Water and fertilizer nitrogen management to minimize nitrate pollution from a cropped soil in southwestern Quebec, Canada. *Water Air Soil Poll* **2004**, *151* (1), 117−134.
(18) Pye, V. I.; Patrick, R. Ground water contamination in the United States. *Science* **1983**, *221* (4612), 713−718.
(19) Duca, M.; Koper, M. T. M. Powering denitrification: the perspectives of electrocatalytic nitrate reduction. *Energy Environ. Sci.* **2012**, *5* (12), 9726−9742.
(20) Chen, G. F.; Yuan, Y.; Jiang, H.; Ren, S.-Y.; Ding, L.-X.; Ma, L.; Wu, T.; Lu, J.; Wang, H. Electrochemical reduction of nitrate to ammonia via direct eight-electron transfer using a copper-molecular solid catalyst. *Nat. Energy* **2020**, *5* (8), 605−613.
(21) Dortsiou, M.; Kyriacou, G. Electrochemical reduction of nitrate on bismuth cathodes. *Electroanal. Chem.* **2009**, *630* (1−2), 69−74.
(22) Katsounaros, I.; Ipsakis, D.; Polatides, C.; Kyriacou, G. Efficient electrochemical reduction of nitrate to nitrogen on tin cathode at very high cathodic potentials. *Electrochim. Acta* **2006**, *52* (3), 1329−1338.
(23) Li, P.; Jin, Z.; Fang, Z.; Yu, G. A single-site iron catalyst with preoccupied active centers that achieves selective ammonia electrosynthesis from nitrate. *Energy Environ. Sci.* **2021**, *14* (6), 3522−3531.
(24) Niu, H.; Zhang, Z.; Wang, X.; Wan, X.; Shao, C.; Guo, Y. Theoretical insights into the mechanism of selective nitrate-to-ammonia electroreduction on single-atom catalysts. *Adv. Funct. Mater.* **2021**, *31* (11), 2008533.
(25) Pan, Y.; Lin, R.; Chen, Y.; Liu, S.; Zhu, W.; Cao, X.; Chen, W.; Wu, K.; Cheong, W. C.; Wang, Y.; Zheng, L.; Luo, J.; Lin, Y.; Liu, Y.; Liu, C.; Li, J.; Lu, Q.; Chen, X.; Wang, D.; Peng, Q.; Chen, C.; Li, Y. Design of single-atom Co-N_5 catalytic site: a robust electrocatalyst for CO_2 reduction with nearly 100% CO selectivity and remarkable stability. *J. Am. Chem. Soc.* **2018**, *140* (12), 4218−4221.
(26) Liu, J.; Jiao, M.; Lu, L.; Barkholtz, H. M.; Li, Y.; Wang, Y.; Jiang, L.; Wu, Z.; Liu, D. J.; Zhuang, L.; Ma, C.; Zeng, J.; Zhang, B.; Su, D.; Song, P.; Xing, W.; Xu, W.; Wang, Y.; Jiang, Z.; Sun, G. High performance platinum single atom electrocatalyst for oxygen reduction reaction. *Nat. Commun.* **2017**, *8*, 15938.
(27) Li, J.; Chen, S.; Quan, F.; Zhan, G.; Jia, F.; Ai, Z.; Zhang, L. Accelerated dinitrogen electroreduction to ammonia via interfacial polarization triggered by single-atom protrusions. *Chem.* **2020**, *6* (4), 885−901.
(28) Tao, H.; Choi, C.; Ding, L.-X.; Jiang, Z.; Han, Z.; Jia, M.; Fan, Q.; Gao, Y.; Wang, H.; Robertson, A. W.; Hong, S.; Jung, Y.; Liu, S.; Sun, Z. Nitrogen fixation by Ru single-atom electrocatalytic reduction. *Chem.* **2019**, *5* (1), 204−214.
(29) Wu, Z. Y.; Karamad, M.; Yong, X.; Huang, Q.; Cullen, D. A.; Zhu, P.; Xia, C.; Xiao, Q.; Shakouri, M.; Chen, F. Y.; Kim, J. Y. T.; Xia, Y.; Heck, K.; Hu, Y.; Wong, M. S.; Li, Q.; Gates, I.; Siahrostami, S.; Wang, H. Electrochemical ammonia synthesis via nitrate reduction on Fe single atom catalyst. *Nat. Commun.* **2021**, *12* (1), 2870.
(30) Zhao, J.; Ren, X.; Liu, X.; Kuang, X.; Wang, H.; Zhang, C.; Wei, Q.; Wu, D. Zn single atom on N-doped carbon: Highly active and selective catalyst for electrochemical reduction of nitrate to ammonia. *Chem. Eng. J.* **2023**, *452*, 139533.
(31) Cheng, X. F.; He, J. H.; Ji, H. Q.; Zhang, H. Y.; Cao, Q.; Sun, W. J.; Yan, C. L.; Lu, J. M. Coordination symmetry breaking of single-atom catalysts for robust and efficient nitrate electroreduction to ammonia. *Adv. Mater.* **2022**, *34* (36), No. 2205767.
(32) Li, J.; Li, M.; An, N.; Zhang, S.; Song, Q.; Yang, Y.; Liu, X. Atomically dispersed Fe atoms anchored on S and N-codoped carbon for efficient electrochemical denitrification. *Proc. Natl. Acad. Sci. U.S.A.* **2021**, *118* (33), No. e2105628118.
(33) Zhu, T.; Chen, Q.; Liao, P.; Duan, W.; Liang, S.; Yan, Z.; Feng, C. Single-atom Cu catalysts for enhanced electrocatalytic nitrate reduction with significant alleviation of nitrite production. *Small* **2020**, *16* (49), No. 2004526.
(34) Yang, J.; Qi, H.; Li, A.; Liu, X.; Yang, X.; Zhang, S.; Zhao, Q.; Jiang, Q.; Su, Y.; Zhang, L.; Li, J. F.; Tian, Z. Q.; Liu, W.; Wang, A.; Zhang, T. Potential-driven restructuring of Cu single atoms to nanoparticles for boosting the electrochemical reduction of nitrate to ammonia. *J. Am. Chem. Soc.* **2022**, *144* (27), 12062−12071.
(35) Xu, G.; Cai, C.; Wang, T. Toward sabatier optimal for ammonia synthesis with paramagnetic phase of ferromagnetic transition metal catalysts. *J. Am. Chem. Soc.* **2022**, *144* (50), 23089−23095.
(36) Xiao, M.; Gao, L.; Wang, Y.; Wang, X.; Zhu, J.; Jin, Z.; Liu, C.; Chen, H.; Li, G.; Ge, J.; He, Q.; Wu, Z.; Chen, Z.; Xing, W. Engineering energy level of metal center: Ru single-atom site for efficient and durable oxygen reduction catalysis. *J. Am. Chem. Soc.* **2019**, *141* (50), 19800−19806.
(37) Geng, Z.; Liu, Y.; Kong, X.; Li, P.; Li, K.; Liu, Z.; Du, J.; Shu, M.; Si, R.; Zeng, J. Achieving a record-high yield rate of 120.9 ug_{NH3} $mg_{cat.}^{-1}h^{-1}$ for N_2 electrochemical reduction over Ru single-atom catalysts. *Adv. Mater.* **2018**, *30* (40), 1803498.
(38) Gu, J.; Li, Z.; He, D.; Yan, X.; Dai, S.; Younan, S.; Ke, Z.; Pan, X.; Xiao, X.; Wu, H. Size-dependent Ni-based electrocatalysts for

https://doi.org/10.1021/acsnano.2c09691
ACS Nano 2023, 17, 3483−3491

selective CO_2 reduction. *Angew. Chem., Int. Ed.* **2020**, *132* (42), 18731−18736.
(39) Wang, Y.; Zhou, W.; Jia, R.; Yu, Y.; Zhang, B. Unveiling the activity origin of a copper-based electrocatalyst for selective nitrate reduction to ammonia. *Angew. Chem., Int. Ed.* **2020**, *59* (13), 5350−5354.
(40) Jia, R.; Wang, Y.; Wang, C.; Ling, Y.; Yu, Y.; Zhang, B. Boosting selective nitrate electroreduction to ammonium by constructing oxygen vacancies in TiO_2. *ACS Catal.* **2020**, *10* (6), 3533−3540.
(41) Wang, J.; Cai, C.; Wang, Y.; Yang, X.; Wu, D.; Zhu, Y.; Li, M.; Gu, M.; Shao, M. Electrocatalytic reduction of nitrate to ammonia on low-cost ultrathin CoO_x nanosheets. *ACS Catal.* **2021**, *11* (24), 15135−15140.
(42) Yang, X.; Ling, F.; Su, J.; Zi, X.; Zhang, H.; Zhang, H.; Li, J.; Zhou, M.; Wang, Y. Insights into the role of cation vacancy for significantly enhanced electrochemical nitrogen reduction. *Appl. Cataly. B: Environ.* **2020**, *264*, 118477.
(43) Li, P.; Jin, Z.; Fang, Z.; Yu, G. A surface-strained and geometry-tailored nanoreactor that promotes ammonia electrosynthesis. *Angew. Chem., Int. Ed.* **2020**, *59* (50), 22610−22616.
(44) Choi, J.; Du, H. L.; Nguyen, C. K.; Suryanto, B. H. R.; Simonov, A. N.; MacFarlane, D. R. Electroreduction of nitrates, nitrites, and gaseous nitrogen oxides: a potential source of ammonia in dinitrogen reduction studies. *ACS Energy Lett.* **2020**, *5* (6), 2095−2097.
(45) Hao, Y. C.; Guo, Y.; Chen, L. W.; Shu, M.; Wang, X. Y.; Bu, T. A.; Gao, W. Y.; Zhang, N.; Su, X.; Feng, X.; Zhou, J. W.; Wang, B.; Hu, C. W.; Yin, A. X.; Si, R.; Zhang, Y. W.; Yan, C. H. Promoting nitrogen electroreduction to ammonia with bismuth nanocrystals and potassium cations in water. *Nat. Catal.* **2019**, *2* (5), 448−456.
(46) Cao, N.; Chen, Z.; Zang, K.; Xu, J.; Zhong, J.; Luo, J.; Xu, X.; Zheng, G. Doping strain induced bi-Ti^{3+} pairs for efficient N_2 activation and electrocatalytic fixation. *Nat. Commun.* **2019**, *10* (1), 2877.
(47) Lv, C.; Yan, C.; Chen, G.; Ding, Y.; Sun, J.; Zhou, Y.; Yu, G. An amorphous noble-metal-free electrocatalyst that enables nitrogen fixation under ambient conditions. *Angew. Chem., Int. Ed.* **2018**, *57* (21), 6073−6076.

https://doi.org/10.1021/acsnano.2c09691
ACS Nano 2023, 17, 3483−3491